Multispectral Images of Ostraca: Acquisition and Analysis

Shira Faigenbaum[a,§,1], Barak Sober[a,§], Arie Shaus[a], Murray Moinester[b], Eli Piasetzky[b], Gregory Bearman[c], Michael Cordonsky[b], Israel Finkelstein[d]

[a] Department of Applied Mathematics, Sackler Faculty of Exact Sciences, Tel Aviv University, Tel Aviv 69978, Israel (alecsan1@ post .tau.ac.il ; baraksov@post.tau.ac.il ; ashaus@post.tau.ac.il)

[b] School of Physics and Astronomy, Sackler Faculty of Exact Sciences, Tel Aviv University, Tel Aviv 69978, Israel (murray.moinester@gmail.com ; eip@tauphy.tau.ac.il ; mcordi@gmail.com)

[c] ANE Image, Pasadena CA 91104 (greg@aneimage.com)

[d] Jacob M. Alkow Department of Archaeology and Ancient Near Eastern Civilizations, Tel Aviv University, Tel Aviv 69978, Israel (fink2@post.tau.ac.il)

§: Both authors contributed equally to this work.

Abstract

We examine how multispectral imaging can be used to document and improve reading of ancient inscriptions. The research focuses on ostraca, texts written in ink on ceramic potsherds. Three corpora of Hebrew ostraca dating to the Iron Age II were imaged in visible and near infrared light using a state-of-the-art commercial spectral imager. To assess the quality of images, we used a new quality evaluation measure which takes into account various contrast and brightness transformations. We show that there exists a wavelength range where the readability of ostraca is enhanced. Moreover, we show that it is sufficient to use certain bandpass filters to achieve the most favorable image. Our study paves the way towards a low cost multispectral method of imaging ostraca inscriptions.

Keywords: visible and near infrared photography, multispectral imaging, ostraca, epigraphy, Hebrew epigraphy, contrast evaluation, potential contrast, CMI.

[1] Tel: +972 3 6406024

1. Introduction

Most of the texts written during the Iron Age in Israel and Judah that survived across the millennia, are ink inscriptions on clay potsherds (ostraca). These ink writings are often partially effaced and blurred. Furthermore, in post-excavation, uncontrolled standard room conditions, the ink of the ostraca fades more rapidly than in the ground (Muros and Hirx, 2004). For preservation and documentation, an optimal procedure is needed for quickly imaging and storing ostraca after excavation. Acquiring the best possible images will aid epigraphers in the process of deciphering these inscriptions.

Multispectral imaging has been researched and used extensively in archaeology (e.g., Liang 2012). Many of these studies focused on ink inscriptions written on parchment (e.g., Bearman and Spiro, 1996; Knox et al., 1997; Easton et al., 2003). A significant improvement in document legibility is sometimes achieved at near infrared (NIR) wavelengths. One may thus conjecture that the optimal ostracon image can likewise be achieved in the NIR (e.g., Rosenbaum and Seger, 1986; Zuckerman, 1997; Bülow-Jacobsen, 2008; Verhoeven, 2008). But this has never been studied in depth.

We employed multispectral imaging in a systematic study of 33 ostraca in order to determine their optimal imaging wavelengths. Each ostracon yielded several images, corresponding to the different wavelengths. Our goal was to find the most legible image among these. For this purpose, we defined and utilized an objective method to evaluate the inscriptions' images readability.

The paper is organized as follows: Section 2.1 gives a concise introduction to digital images; Section 2.2 exemplifies pitfalls of existing image quality measures and presents an alternative measure; Section 3 describes the ostraca imaging experiment and discusses the results; the paper concludes with Section 4, which presents a low cost multispectral system and a recommended imaging procedure.

2. Quality assessment of an image

2.1 Basic digital images concepts

The standard digital camera produces an RGB color image. This image consists of three color channels that correspond to different ranges of visible light (red: 600-700

nm, green: 500-600 nm, blue: 400-550 nm)[2]. Each of these color channels is a matrix of numbers (pixel values) representing the light intensity reflected from each point in space. The intensity value for each pixel (for eight bit images) ranges between 0 and 255, where 0 indicates no reflection and 255 indicates maximal reflection.

From the color image, one can also create a gray level image by averaging the RGB channels. A pixel with value 0 is colored black, while 255 is white (Figure 2.1). Additionally, each channel can be treated as a separate gray level image.

Figure 2.1: *Gray level scale (0-255)*

In multispectral imaging, the outcome (*spectral cube*) consists of many channels (denoted here as *λ-images*), each taken at a different wavelength (λ). In our case, the cube contains 51 channels (Figure 2.2). As described above, each of these channels can also be viewed as a gray level image in itself, representing the light reflectance measured through a specific bandpass filter. For a more in depth discussion regarding MS techniques see (Kubik, M., 2007).

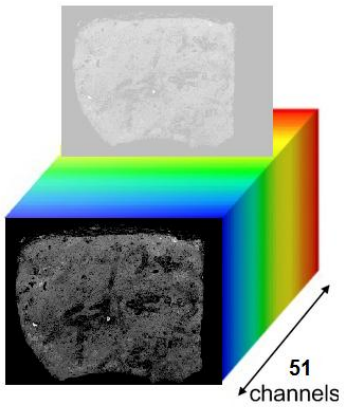

Figure 2.2*: An illustration of a multispectral cube.*

2.2 Assessing the quality of a digital image

The problem of choosing the "best" image among a given set of images is not well defined, as evaluating the quality of an image can be done based on a variety of

[2] These channel bandpasses are just an approximation, and are different for each camera. More precise values of these ranges for our camera, Canon 450D, are given at: http://www.maxmax.com/ndvi_camera_technical.htm (last accessed: 05.12.2011)

criteria. Since image quality is a subjective property, the most natural way to assess its quality is by eye. Alas, this raises several problems.

As the human mind responds differently to changes of color in bright and dark images (Weber–Fechner law [Fechner 1860]), it is difficult to decide whether a bright image possesses a good quality. Moreover, the legibility of a seemingly unappealing image may be significantly enhanced by brightness and contrast manipulations (Figure 2.3), which can be carried out with available image processing software (such as Photoshop, GIMP, etc.). Numerous manipulations ought to be attempted for each image, in order to bring it to the most legible state. This problem is further intensified by the fact that in the course of our analysis, we had to evaluate the quality of about 1500 images. Such a manual comparison task would have been practically impossible.

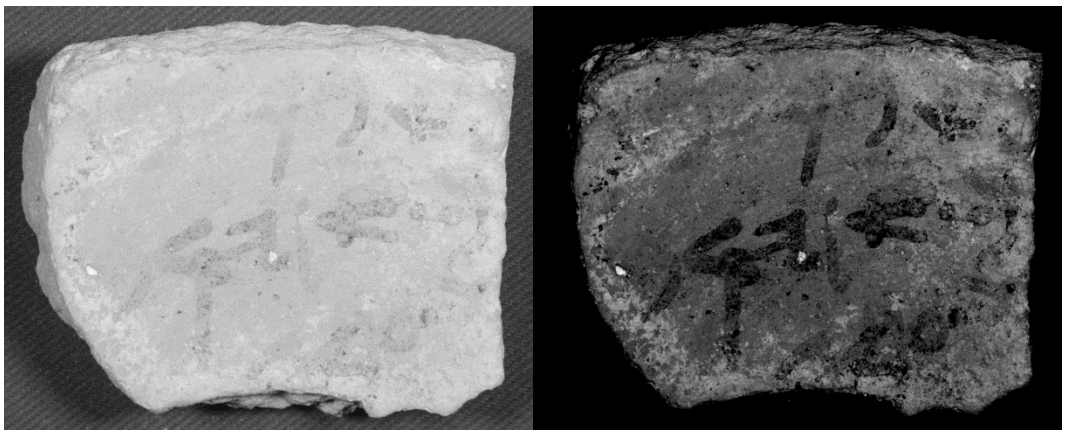

Figure 2.3: *Two images of ostracon No. 1 from Horvat Radum;*
original (left) and after brightness and contrast manipulations (right).
The original image contains more information than the modified one, since the brightness and contrast manipulations can only reduce the gray scale range. Although the differences between foreground and background appear more evident to the human eye in the modified image, the quality of the original image is actually higher.

As stated above, the quality evaluation of an image can be carried out in many ways. Commonly used measures (such as: Michelson, Weber, RMS) evaluate the contrast between foreground and background (ink and clay in our case) (Peli, 1990). But these measures are themselves sensitive to standard manipulations (i.e., brightness and contrast transformations) performed with the available image processing software. A suggested solution to this problem uses the concept of *potential contrast* (Faigenbaum et al., forthcoming). The potential contrast of a given image is the maximal contrast achievable by such manipulations. The image with the best potential contrast can be

selected out of a given set of images. We will denote the potential contrast measure as $PC(I)$ (where I is an image).

In order to calculate the potential contrast of an image, the following steps are performed (demonstrated in Figure 2.4):

i. Given an inscription image (Figure 2.4a), areas of foreground (ink) and background (clay) are sampled manually (Figure 2.4b).

ii. The distributions of ink and clay gray levels, denoted respectively as $p_F(t)$ and $p_B(t)$, are derived using the sampled areas (Figure 2.4c).

iii. New values (255 or 0) are assigned to each pixel of the original image according to these distributions, in the following fashion:

- For a pixel with gray level *t*, if the probability for "ink" is greater than (or equal to) the probability for "clay" (i.e., $p_B(t) \le p_F(t)$), its new value is 0.
- If, on the other hand $p_B(t) > p_F(t)$, the pixel value is set to 255 (Figure 2.4d).

This procedure produces a new, black and white, image (Figure 2.4e).

iv. The last step involves averaging the *new* values of the ink and clay sampled areas (Figure 2.4f). Avg_F (Avg_B) denotes the average over the ink (clay) sampled pixels. By using these averages, the potential contrast (PC) is defined as:

$$PC(I) = Avg_B - Avg_F$$

Intuitively, the calculation of the potential contrast brings the pixel values of the sampled areas to their extreme. For a pixel, which probably belongs to the background, the value is set to 255, while the likely foreground pixels are set to 0. It can be proved that this way, the difference between the foreground and the background is brought to its maximum. For a more detailed discussion regarding the concept of potential contrast, see Appendix B.

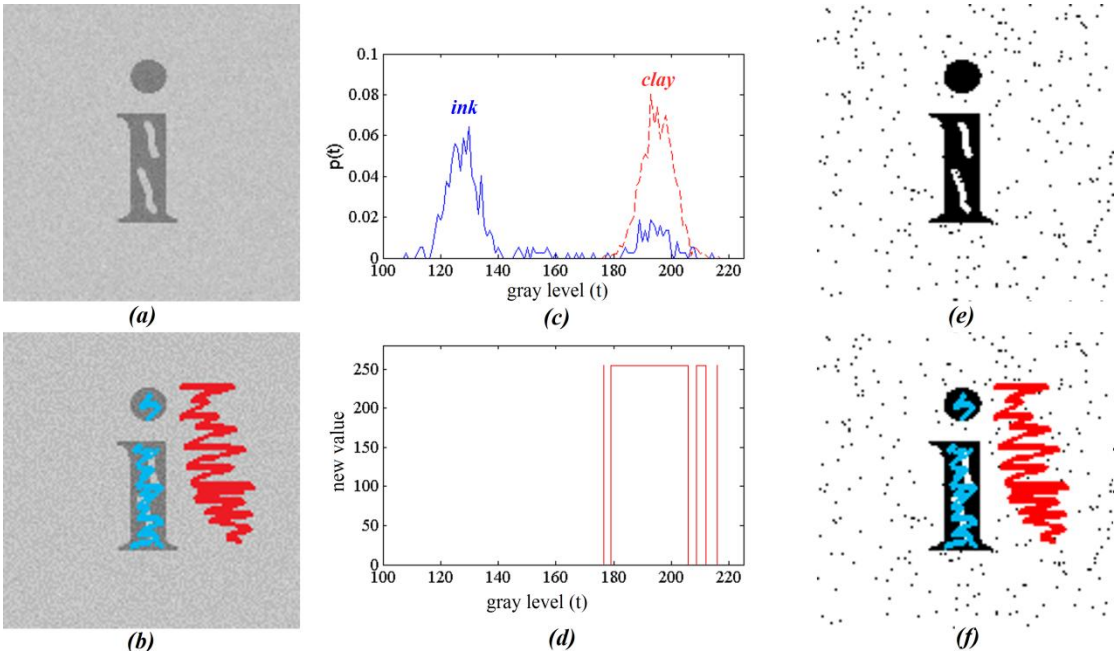

Figure 2.4: *Applying the algorithm to an artificially constructed example: (a) the original image; (b) manually sampled areas: blue-foreground, red-background; (c) a plot of the two resulting distributions: blue (solid)-foreground, red (dashed)-background; (d) setting each pixel value with either 255 or 0 according to* $p_F(t)$ *and* $p_B(t)$*; (e) the output image after the pixel value changes (255 - white, 0 - black); (f) the sampled areas superimposed on the new image. In this example* $PC(I) = 239$*. Note that although the sampled ink pixels (b) include an effaced area (to imitate a real case), this inclusion has little effect on the PC value.*

Using the above procedure on a spectral cube, the best λ-image (I_λ) is the one corresponding to the highest $PC(I_\lambda)$ value. This chosen λ-image can produce the best contrasted image with respect to the sampled areas.

3. Experiment, analysis and results

3.1 Experiment description

The experiment included imaging with both visible and infrared light. Spectral data of 33 ostraca with black ink were obtained using a state-of-the-art commercial multispectral imager.[3] The imaged ostraca were excavated at Horvat Radum, Horvat Uza and Tel Malhata (Beit-Arieh, 2007) – Iron Age sites located in the Beersheba Valley and its surroundings (for a detailed list of ostraca, see Appendix C).

[3] CRI Nuance VariSpec SNIR-10 (short/near infrared) LCTF (liquid crystal tunable filter) multispectral imager, fitted with a CoastalOpt UV-VIS-IR 60mm apochromatic lens.

The spectral imager covers 440-960 nm with image acquisition bandwidths of approximately 20 nm and overlap of 10 nm between consecutive images. The bandwidth of the first image is therefore centered at λ = 450 nm and covers the range 440-460 nm, the second image is centered at λ = 460 nm and covers the range 450-470 nm, and so on. The acquisition results in a *spectral cube* consisting of 51 *λ-images*, corresponding to different central wavelengths. For each *λ-image* the exposure was set separately to fill the camera's sensor up to ~75% of the full pixel well depth. Thus, different images contain the same dynamic range.

In order to correct the ostraca images for non-uniform lighting, we carried out a flat-field procedure, as described in (Emerson and Little, 1999). For more details, see Appendix A.

After acquiring the ostraca images, a detailed analysis (described in Section 3.2) was performed in order to decide on the most favorable *λ-image*. The analysis was based upon the above-mentioned quality evaluation measure.

3.2. Multispectral cube analysis

For each ostracon, areas of ink and clay were marked (e.g., Figure 3.1). The areas were the same for the entire spectral cube. The $PC(I_\lambda)$ value was then calculated for each λ-image in the cube. The measurements taken from Horvat Radum ostracon No. 1 cube are presented in Figure 3.2.

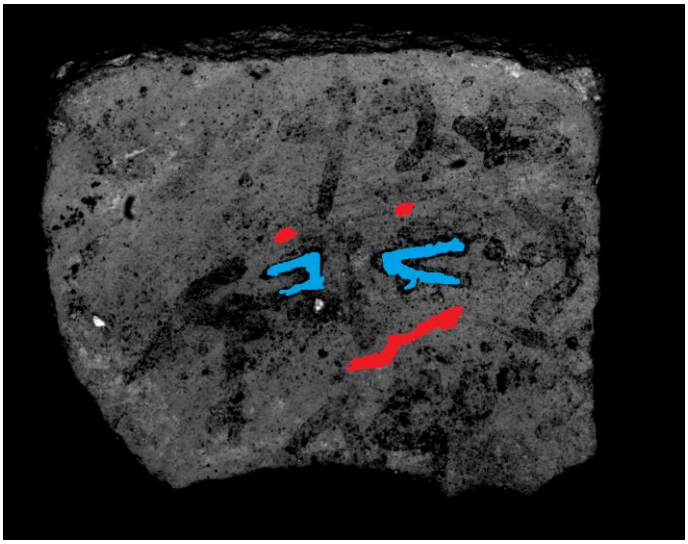

Figure 3.1: *Sampled areas on ostracon No. 1 from Horvat Radum. Blue - ink area; red - clay area.*

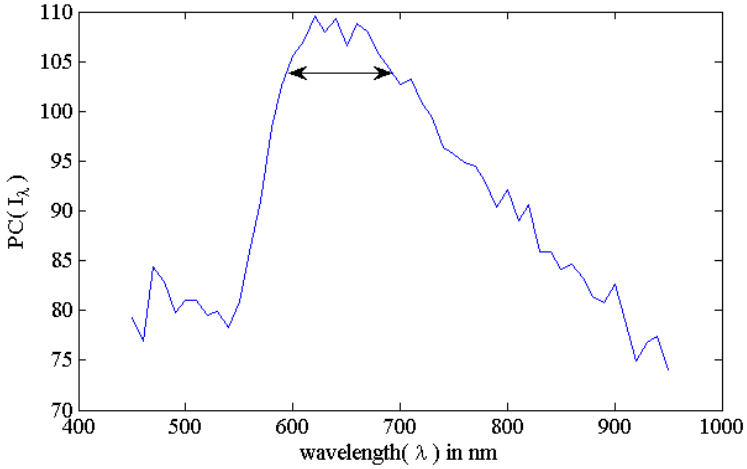

Figure 3.2: *$PC(I_\lambda)$ as a function of central wavelength λ.*

The peak range is marked by the arrows.

The graph relies on the ink and clay sampled areas as presented in Figure 3.1.

It has been verified empirically that λ-images corresponding to 5% less than the $PC(I_\lambda)$ maximum still result in images almost identical to the optimal one (e.g., see Figure 3.3 left and center). On the other hand, λ-images corresponding to significantly lower $PC(I_\lambda)$ values are substantially less legible (see Figure 3.3 right). We shall therefore set a threshold at 95% of the maximum $PC(I_\lambda)$ value. The range of λ-images giving a $PC(I_\lambda)$ value above that threshold will be denoted as "*peak range.*"

In Figure 3.2, the $PC(I_\lambda)$ maximum value (*peak*) is reached at 620 nm. The peak range is 600-690 nm, which is quite wide (90 nm). As will be shown later, this is a typical case.

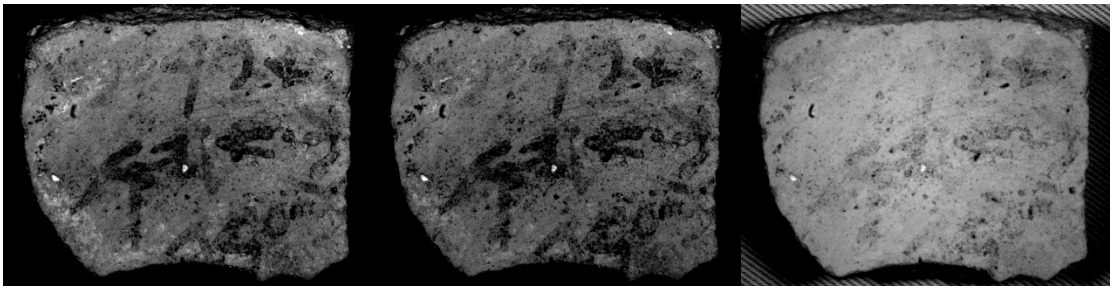

Figure 3.3: *Images from the spectral cube of Horvat Radum ostracon No. 1*

Left: optimal image at $\lambda = 620nm$; center: image at $\lambda = 690nm$ (5% less than the $PC(I)$ maximum); right: the worst image at $\lambda = 950nm$. All three images were slightly improved by using brightness and contrast post processing.

As described above, a full color image is a combination of three channels, induced by different bandpass filters (red: 600-700 nm, green: 500-600 nm, blue: 400-550 nm). Since these filters cover a very wide range, it is likely that they contain data from outside the peak range. Empirically, λ-images from the peak range are more legible than a full color image taken with a standard digital camera. The same applies to a full color image converted to a gray scale image (e.g., Figure 3.4 and 3.5).

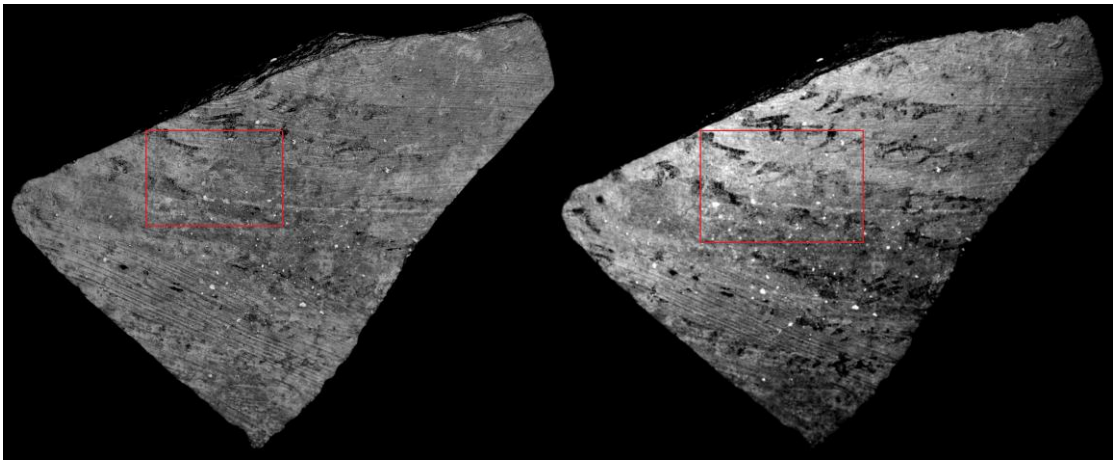

Figure 3.4: *Ostracon No. 3 from Horvat Uza. Left: a full color image (approximately 400-700 nm) converted to gray scale; right: a λ-image from the peak range (710nm).*

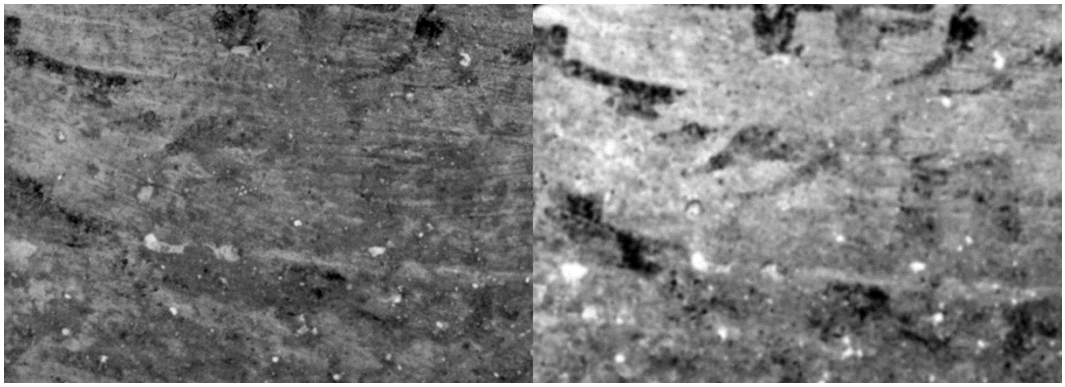

Figure 3.5: *Detail of ostracon No.3 from Horvat Uza. Left: a full color image (approximately 400-700 nm) converted to gray scale; right: a λ-image from the peak range (710 nm).*

3.3. Results

In our experiment, we acquired spectral cubes of 33 black ink ostraca. In cases where non-uniform ink degradation was observed, different sections (of the same ostracon) were sampled, each section representing a different level of degradation. For example,

in Horvat Radum ostracon No. 1, we sampled each line separately (i.e., 3 sections). In total we have sampled 59 different sections. Figure 3.6 shows the distribution of the peak ranges for each section treated.

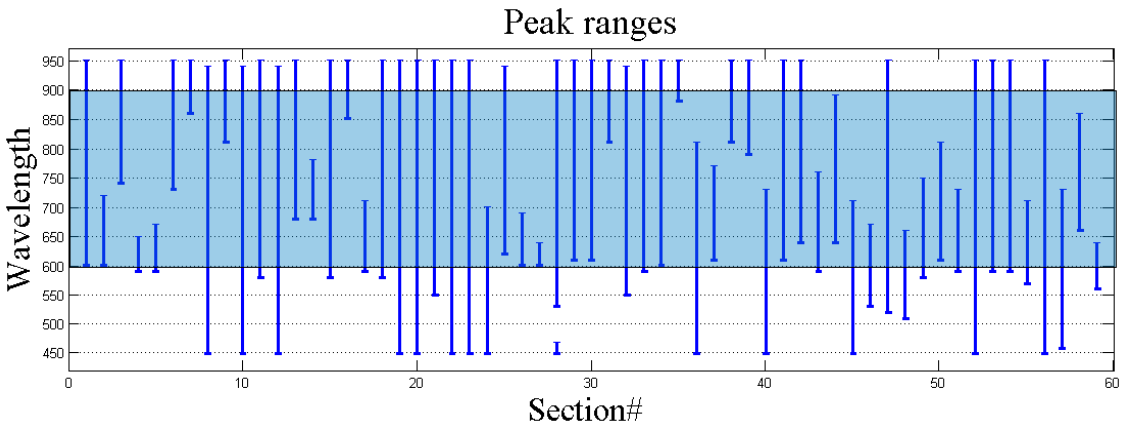

Figure 3.6: *Summary of 59 sampling sections.*

The vertical lines represent the peak ranges.

The wavelength range marked in blue has a meaningful intersection with all the peak ranges.

In 52 out of the 59 sections (about 88%), the peak range is wider than 100 nm (Figures 3.6 and 3.7). As a result, in order to acquire the most legible image, we can use bandpass filters having a relatively wide range (yet narrow enough to be contained within the particular peak range).

Contrary to the belief that the near infrared (NIR) range is the most beneficial for ostraca imaging (Bülow-Jacobsen, 2008), this is not always the case. As can be seen in Figure 3.6, all of the peak ranges intersect with the wavelength range of 600-900 nm. Therefore, adding a safety factor, the range that needs to be covered is 550-950 nm. As it cannot be foreseen in advance which of the wavelengths will result in the best image, it is important to take images covering a large part of the spectrum.

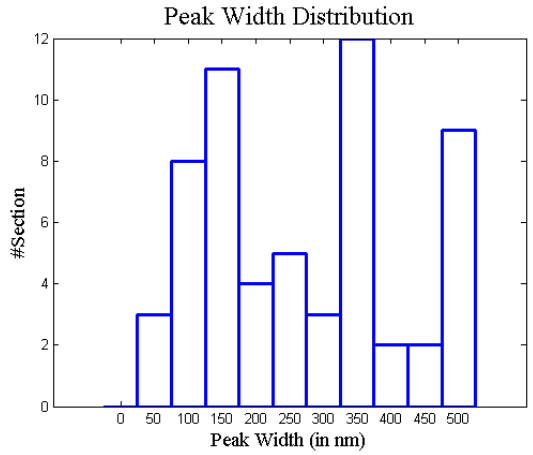

Figure 3.7: *Peak width distribution.*

Another interesting fact is that in nine sections, the peak ranges were nearly 450-950 nm. This means that each λ-image is as legible as the others. This phenomenon indicates that in these cases, the written letters are especially distinct.

Moreover, we found a clear correlation between wide peak ranges and well preserved ink. As the ink is better preserved, the $PC(I_\lambda)$ value approaches 255 (this fact follows from the definition of the measure). Figure 3.8 shows the correlation between the wide peaks and the $PC(I_\lambda)$ value. As can be seen, the very wide peaks are associated with high $PC(I_\lambda)$ values (i.e., well preserved ink), while relatively narrow peaks (around 100 nm) are associated with low $PC(I_\lambda)$ values (i.e., less legible sections).

In other words, the less legible sections correlate with narrow peak ranges. In such cases, imaging outside the peak ranges is especially disadvantageous. Accordingly, the utilized bandpass filters should not be too wide.

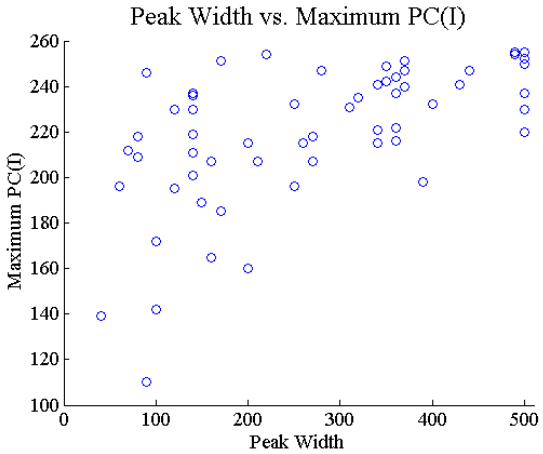

Figure 3.8: *Scatter plot showing the relation between the* $PC(I_{\lambda})$ *measurements and the width of the peak ranges.*

It may be conjectured that by considering the entire cube as a whole, one might gain more information than by looking at each image separately. We, therefore, employed Principal Component Analysis (PCA) on each of the spectral cubes. However, no significant improvement was observed. In only two cases was a minor improvement seen in one of the PCA components.

X-ray fluorescence (XRF) was employed to identify chemical elements present in the black ink of several ostraca used in this study. The ink is not iron-based like iron-gall, and was therefore presumed to be based on a carbonaceous pigment (Nir-El et al., forthcoming). Thus, the results presented above relate to carbon based ink on clay shards.

In addition to the 33 black ink ostraca, we examined a red ink ostracon. The red ink ostracon has an optimal wavelength of 570 nm and a peak width of 30 nm. However, since there were no additional red ink ostraca available, we cannot establish a general conclusion regarding the optimum method to image them.

4. Building an imaging system and the recommended procedure

Since the ink of the ostraca tends to fade over time, it is important to acquire the best possible imagery in close proximity to the excavation. Proper ostraca images will aid the present and future epigraphers in their task of analyzing and deciphering the inscriptions. As shown above, multispectral imagery is advantageous for the task of ostraca documentation. On the other hand, typical multispectral imaging systems tend to be expensive and therefore may not be a part of the standard excavation equipment. We suggest an alternative, low-cost multispectral solution, and a suitable procedure of acquiring the optimal imagery.

4.1 Building an imaging system

Based on the results presented in Section 3, we suggest a construction of a low cost multispectral imaging system. The system comprises a modified digital camera along with a set of bandpass filters.

Using a bandpass filter, the resulting image records the intensity induced by the wavelengths passing through the filter, combined with the sensitivity of the camera sensor. As seen above, including non-optimal wavelengths reduces the image contrast and legibility. Therefore, it is important to use a filter whose bandpass range is *contained* in the peak range of the ostracon (e.g., Figure 4.1).

As mentioned previously, we found that the $PC(I_\lambda)$ peaks tend to have bandwidths larger than 100 nm. This allows the use of relatively wide bandpass filters. If we cover the entire spectrum with bands of 50 nm (with no overlapping), there should exist a specific band that is completely contained in the peak range. This assures that we acquire an image consisting primarily of optimal wavelengths.

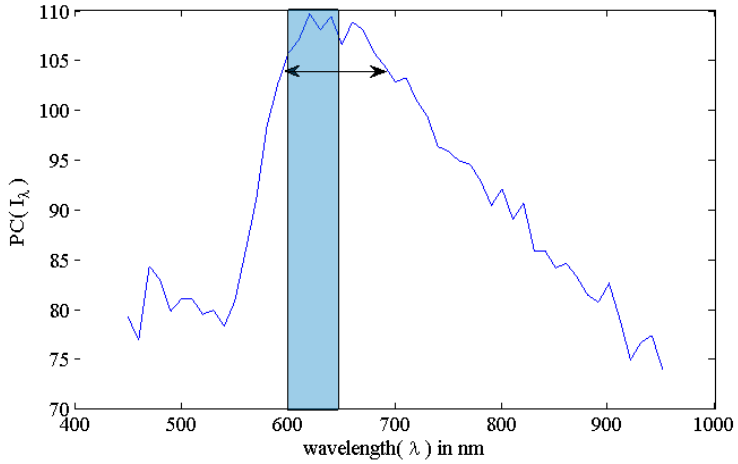

Figure 4.1: *$PC(I_\lambda)$ of ostracon No. 1 from Horvat Radum. The arrows show the peak range, while the marked area represents the wavelength region passing through an ideal bandpass filter having range 600-650 nm.*

As explained in Section 3.3, we can limit ourselves to image the range 550-950 nm. It is possible to order an ideal set of filters, having transmission central wavelengths 575, 625, 675, 725, 775, 825, 875, 925 nm, and 50 nm bands, for the purpose of covering this range. It is, however, more cost effective to use non-ideal "off the shelf" filters (for a detailed suggestion, see Appendix A).

A standard digital camera image contains three channels (R, G and B). Therefore, an image taken with a specific bandpass filter results in three different images, where each of these channels is now filtered. For example, image G would be a bandpass image of the green sensitivity range (500-600 nm), intersected with the

range of the bandpass filter.[4] If one takes an image using a bandpass filter of 500-550 nm, among the three images, images G and B would contain relevant data, while R image would mostly contain noise (Figure 4.2). Therefore, in this case, image G can be used by itself. It should be noted that since we focus on the range of 550-950 nm, the B channel (400-550 nm) can be ignored entirely.

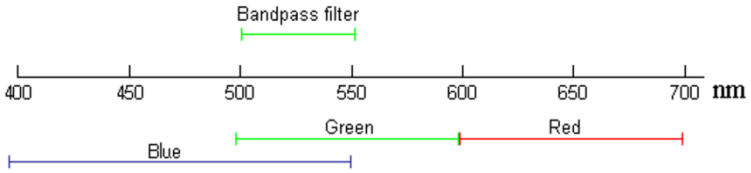

Figure 4.2: *An illustration of the intersection between a range of a bandpass filter and the three channels sensitivity range. Below the axis – the sensitivity range of each channel; above the axis – the range of the bandpass filter. When using such a filter, the resulting R image will mostly contain noise.*

As stated above, the sampling areas for calculating the $PC(I_\lambda)$ have been the same for the entire cube. This was performed based on the assumption that the images that comprise the cube are precisely aligned. However, it is possible that the images resulting from the described system will only be aligned roughly. In this case, the sampling of ink and clay should be carried out more carefully.

4.2 The recommended imaging procedure

Based on our studies, we define a procedure to obtain optimal images of ostraca, using the system described in Section 4.1.

With each filter repeat the following steps:

i. Take an image of the ostracon, and extract the relevant channels (red or green).
ii. (optional) Take a gray card image and perform flat fielding (as described in Appendix A).

After acquiring the various images, take one of the following steps:

- If possible, calculate the $PC(I_\lambda)$ of the images' values and choose the images within the peak range. Use image processing software (Photoshop, ImageJ, GIMP, etc.) to adjust the contrast and brightness of these images.
- Otherwise, start with adjusting the contrast and brightness of the various images (using image processing software). Then select manually one or several favorable images.

[4] More accurately, this is a convolution of the two sensitivities.

If a multispectral system is not available, one may compare the red (~600-700 nm), green (~500-600 nm), blue (~400-550 nm) and full color images. In order to improve the readability of old digital images of ostraca, one should look at the different color channels separately. According to the results presented above, the red channel will most likely be the best choice between these possibilities, as was previously observed (Bülow-Jacobsen, 2008).

5. Summary

Since the ink on ostraca fades over time, it is important to obtain the best possible imagery soon after the excavation. We examine how multispectral imaging (infrared and visible light) can be used to document and improve reading of ostraca. A low cost multispectral system and an optimized procedure to acquire ostraca images are proposed.

In the course of our multispectral imaging experiments, we encountered several examples where the broadly-accepted old readings of inscriptions need to be changed. These results will be published elsewhere.

It should be noted that although we only studied ostraca, the implications for manuscripts and works of art could be significant. The methodology and system presented above can be applied to several fields of archaeological imaging. This, of course, requires further study.

This research is part of a large program aimed at digitizing and analyzing Iron Age Hebrew ostraca utilizing computer science methodologies (Faigenbaum et al. forthcoming; Shaus et al., 2012a; Shaus et al., 2012b; Shaus et al., forthcoming; Finkelstein et al., 2012). Producing optimal digital images of ostraca is the first phase in this project.

6. Acknowledgements

The research leading to these results has received funding from the Israel Science Foundation – F.I.R.S.T. (Bikura) Individual Grant no. 644/08. The research was also partially funded by the European Research Council under the European Community's Seventh Framework Programme (FP7/2007-2013)/ERC grant agreement no. 229418, and by an Early Israel grant (New Horizons project), Tel Aviv University.

We thank Itzhaq Beit-Arieh and Liora Freud for allowing us to image the ostraca collection from their excavations; and David Levin and Eli Turkel for assisting with the analysis. The kind help of our ERC coordinator Shirly Ben-Dor Evian is appreciated. We thank Cambridge Research & Instrumentation, Inc. (CRI, http://www.cri-inc.com/index.asp) for the loan of their spectral imager for this project. Gregory Bearman began working with the Tel Aviv University Group while a Fulbright visiting scholar at Tel Aviv University in 2011.
Arie Shaus is grateful to the Azrieli Foundation for the award of an Azrieli Fellowship.

Appendix A

Building the low cost imaging system

Based upon the conclusions described above, a low cost multispectral imaging system, designed for ostraca, was built. In what follows, we give a detailed description of this system. In general, the system comprises a modified digital camera (IR cut filter removed) and a set of bandpass filters.

We used a modified Canon SLR 450D digital camera, and a Tamron SP AF90mm F/2.8 Di 1:1 Macro lens. The internal Canon IR Cut filter was removed by Lifepixel (weblink [1]) and replaced with transparent glass having the same refractive index. The converted camera has useful quantum efficiency from about 400 nm to 1000 nm (weblinks [2, 3]), which follows from the characteristics of the CMOS imaging chip sensor. As a result, to achieve correct color balance for normal (not infrared) imaging, an external color correction filter (weblink [4]) had to be used.

Purchasing an ideal set of filters for this imaging system is expensive; we therefore used nine "off the shelf" filters. Five filters were produced by MidOpt (weblink [5]). These have transmission centers at 590, 635, 660, 695 and 735. Two filters were produced by Omega (weblink [6]), with transmission centers at 775 and 890, and two by Maxmax (weblink [4]), with transmission centers at 830 and 940. All of the filters' bandwidths are 40 up to 70 nm. Figure A.1 shows the coverage of the range 550-950 nm, using these low cost filters.

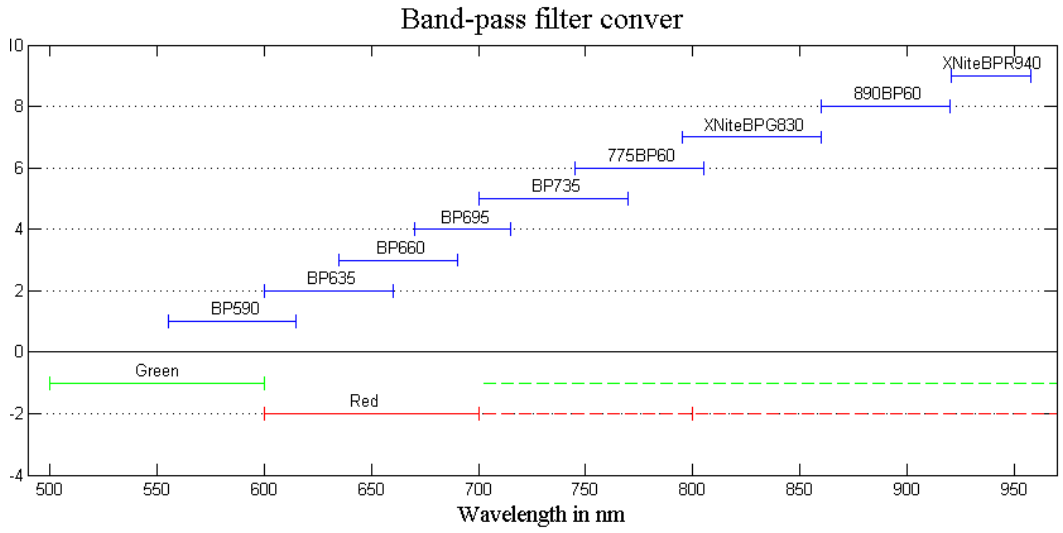

Figure A.1: *Above the axis: off the shelf filters covering the complete range, each with a window of approximately 60 nm. Below the axis: the sensitivity of the different channels in the camera (green and*

red respectively). After removing the IR blocker, the sensitivity of the red and green channels extends up to 1000 nm, shown as a dashed line.

In order to correct the ostraca images for non-uniform lighting, a flat-field procedure should be carried out. The procedure is based on two steps: (a) The spectral cube of the digital gray card (such as WhiBal white balance reference gray card, weblink [7]) must be taken to measure the combined effects of illumination and the imager's spectral sensitivity. (b) Each ostracon's λ-image is normalized with respect to the matching gray card λ-image, to obtain the absolute reflectance (Emerson and Little, 1999).

Measuring the reflectance of the card reveals a slight drop (5%) in the response from 450 nm to 950 nm. Such a minor drop should not affect the results presented above. Furthermore, the images were all taken with the same level of exposure and uniform illumination.

Appendix B

The proliferation of existing image processing software makes it easy to apply various gray level transformations to ostraca imagery. Therefore, when trying to select the best image out of a given set, one has to consider all the *potential images* that can be produced from each image by using such transformations (see Figure B.1). Accordingly, the most favorable image should be the one that bears the potential of producing the optimal image by further manipulations.

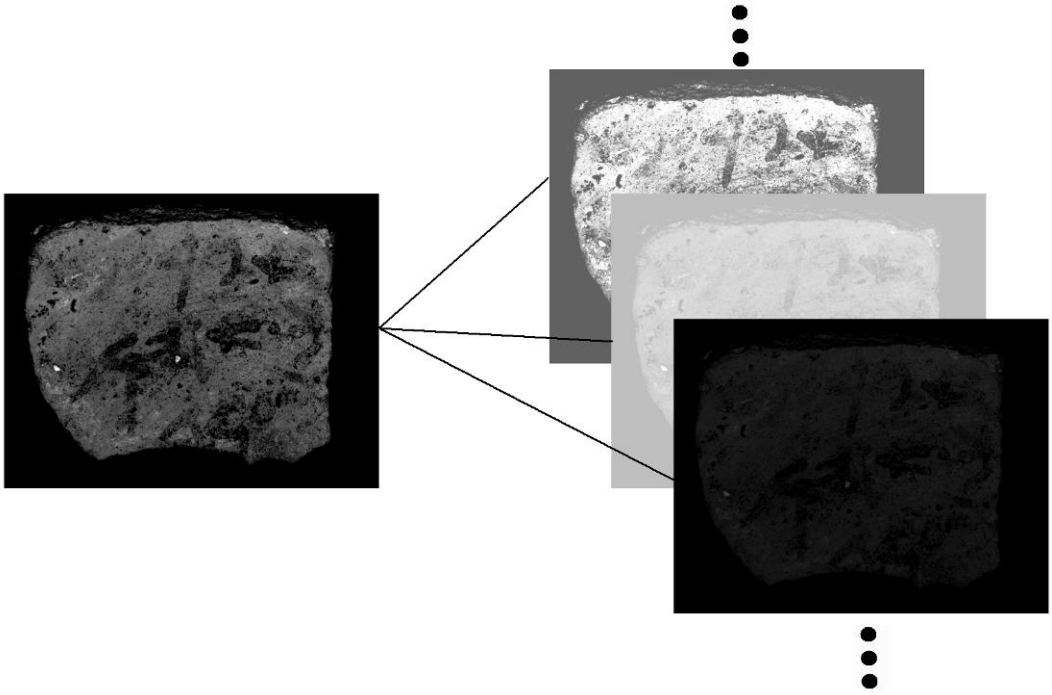

Figure B.1: *An illustration of a set of potential images produced from an image of ostracon No. 1 from Horvat Radum.*

Had we known how to produce the best potential image for each image in the original set, we could have evaluated them instead of the originals. It should be noted that finding such an optimal transformation relies on the image quality measure being used.

As stated above, there are various ways to assess the quality of images. Commonly used measures (such as Michelson, Weber, RMS) try to evaluate the contrast between foreground and background (ink and clay in our case) (Peli, 1990). Another very simple yet efficient contrast measure, developed and tested in (Shaus et al., 2012a; Shaus et al., forthcoming) for the purpose of historical documents analysis, is the CMI (clayness minus inkness) index defined as:

$$CMI = \mu_B - \mu_F$$

where μ_B and μ_F are respectively the averages of the background (clay) and foreground (ink) pixel values.

In (Faigenbaum et al., forthcoming), we show that one may find for each image *I*, the optimal gray level transformation *g*, with respect to the CMI index. The *potential contrast* is, in fact, the CMI value of the potential image created by applying this transformation. We denote it as *PC(I)*:

$$PC(I) = CMI(g(I))$$

Thus, it is assured that the image with the maximum *PC(I)* value is the one that bears the potential of being the best image (with respect to the CMI measure).

In order to calculate the CMI of an image, we have to manually sample the ink and clay populations (see Figure 3.1). The sampled areas are used to derive the gray level empirical distributions of ink (foreground) and clay (background), denoted as $p_F(t)$ and $p_B(t)$ respectively (see Figure B.2 left).

$$\sum_{t=0}^{255} p_F(t) = \sum_{t=0}^{255} p_B(t) = 1 \quad , \quad 0 \le p_F(t), p_B(t) \le 1.$$

The optimal gray level function is found to be:

$$g(t) := \begin{cases} 0 & p_F(t) \ge p_B(t) \\ 255 & p_F(t) < p_B(t) \end{cases}$$

An example of such a function based on the populations presented in Figure B.2 left, can be seen in Figure B.2 right.

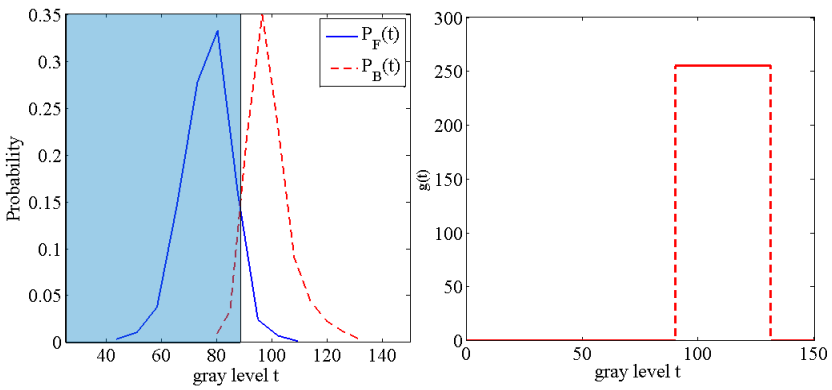

Figure B.2: *Left: Example of the empirical distributions of clay and ink ($p_B(t)$ and $p_F(t)$) as a function of gray level t. Right: The graph of the function g , produced from these distributions.*

The intuition behind the definition of *g* comes from the following facts: if it is more probable that a pixel belongs to the background, then it is preferred to assign to it the maximal value (255). On the other hand, if it is more probably ink, then the minimal value (0) is assigned. As the CMI measures the difference between the average values of the two sampled populations, this function will indeed maximize its value. For a detailed proof regarding this matter see (Faigenbaum et al., forthcoming).

Note that the definition of PC as $PC(I) = CMI(g(I))$ thus results in:

$$PC(I) = Avg_B - Avg_F$$

where Avg_F and Avg_B denotes the average over ink and clay sampled pixels respectively. This is identical to the definition given in Section 2.2.

Appendix C

Table C.1 List of the ostraca from Horvat Radum, Horvat Uza and Tel Malhata (Beit-Arieh, 2007) that were imaged in the course of the experiments described in this paper.

	Corpus	Inscription Number	Reg. No	Locus/Room
1	Horvat Radum	1	4013	Room 205
2	Horvat Radum	2	4020/1	Locus. 308
3	Horvat Radum	4	1009	Locus. 110
4	Horvat Uza	2	1343/2	Locus. 187
5	Horvat Uza	3	2080/1	Room 221 Complex 780
6	Horvat Uza	4	5171/1	Room 567 of Structure 572
7	Horvat Uza	8	1538/1	Locus. 336
8	Horvat Uza	9	1538/2	Locus. 336
9	Horvat Uza	11	2219/1	Room 265 Complex 780
10	Horvat Uza	12	1562	Locus. 318
11	Horvat Uza	13	1690/1	Locus. 324
12	Horvat Uza	15	2331	Room 703 Structure 937
13	Horvat Uza	20	2486.1	Room 741 Building 937
14	Horvat Uza	21	2173/3	Room 1253 Complex 780
15	Horvat Uza	22	4544	Room 1342
16	Horvat Uza	26	4205/1	Room 684 Building 1342
17	Horvat Uza	27	4523	Room 759 Complex 937
18	Horvat Uza	29	4397	Room 397 Complex 927
19	Horvat Uza	30	4522	Room 1341
20	Horvat Uza	31	4435	Locus. 1315
21	Horvat Uza	32	4483/1	Room 1341
22	Tel Malhata	3	3559/1	Locus1510
23	Tel Malhata	4	4189/1	Locus 1564
24	Tel Malhata	4	4189/2	Locus 1564
25	Tel Malhata	5	4264/2	Locus 1564
26	Tel Malhata	6	4189/2	Locus 1564
27	Tel Malhata	7	4190/1	Locus 1569

28	Tel Malhata	8	4264/1	Locus 1564
29	Tel Malhata	12	1071/1	Locus 825
30	Tel Malhata	13	3704/1	Locus 1512
31	Tel Malhata	19	403/1	Locus 603
32	Tel Malhata	17	1240/1	Locus 913
33	Tel Malhata	18	1076/1	Locus 808

Table C.1: *The list of ostraca examined in this research.*

References:

Bearman, G.H., Spiro, S.I., 1996. Archaeological applications of advanced imaging techniques. The Biblical Archaeologist 59, 56–66.

Beit-Arieh, I., 2007. Horvat 'Uza and Horvat Radum: Two Fortresses in the Biblical Negev. Emery and Claire Yass Publications in Archaeology, Tel Aviv.

Bülow-Jacobsen, A., 2008. Infra-red Imaging of Ostraca and Papryi. Zeitschrift für Papyrologie und Epigraphik Vol 165, pp. 175-185.

Easton, R.L., Jr., Knox, K.T., Christens-Barry, W.A., 2003. Multispectral imaging of the Archimedes palimpsest. Applied Imagery Pattern Recognition Workshop, 2003. Proceedings. 32nd , pp. 111- 116, 15-17.

Emerson, G.P., Little, S.J., 1999. Flat-Fielding for CCDs in AAVSO Observations. I. J. AAVSO Vol 27, pp. 49-54.

Faigenbaum, S., Shaus, A., Sober, B., Piasetzky, E., Turkel, E., Moinester, M., Potential Contrast Evaluation - the Best of All Possible Images (to be published).

Fechner, G.T., 1860. Elements of Psychophysics, in: Rand, B. (Ed), Langfeld, H.S. (Trans), The classical psychologists: Selections illustrating psychology from Anaxagoras to Wundt. Houghton Mifflin Company, Boston, 1912, pp. 66-75.

Finkelstein, I., Boaretto, E., Ben Dor Evian, S., Cabanes, D., Cabanes, M., Eliyahu, A., Faigenbaum, S., Gadot, Y., Langgut, D., Martin, M., Meiri, M., Namdar, D., Sapir-Hen, L., Shahack-Gross, R., Shaus, A., Sober, B., Tofollo, M., Yahalom-Mack, N., Zapassky, L., Weiner, S., 2011. Reconstructing Ancient Israel: Integrating Macro- and Micro-archaeology (in press).

Fischer, C., Kakoulli, I., 2006. Multispectral and hyperspectral imaging technologies in conservation: current research and potential applications. Reviews In Conservation, Vol 6, pp. 3-16.

Fredlund, G., 2007. Digital infra-red photography for recoding painted rock art. Antiquity, Vol 81, pp. 733-742.

Knox, K.T., Johnston, R., Easton, R.L., Jr., 1997. Imaging The Dead Sea Scrolls. Optics & Photonics News 8(8), pp. 30-34.

Kubik, M., 2007. Physical Techniques in the Study of Art, Archaeology and Cultural Heritage, Amsterdam, Vol 2, pp. 199-259.

Liang, H., 2012. Advances in multispectral and hyperspectral imaging

for archaeology and art conservation. Applied Physics A: Materials Science & Processing, Vol 106(2), pp. 309-323.

Michelson, A.A., 1927. Studies in Optics. University of Chicago Press.

Muros, V., Hirx, J. 2004. The Use of Cyclododecane as a Temporary Barrier for Water-Sensitive Ink on Archaeological Ceramics during Desalination. Journal of the American Institute for Conservation Vol 43, pp. 75-89.

Nir-El, Y., Goren, Y., Piasetzky, E., Moinester, M., Sober, B., forthcoming. X-ray fluorescence (XRF) measurements of red ink on a Tel Malhata ostracon. Tel Malhata A Central City in the Biblical Negev, Itzhaq Beit-Arieh (ed).

Peli, E., 1990. Contrast in complex images. J. Opt. Soc. Am. A 7, pp. 2032-2040.

Rosenbaum, J., Seger, J.D., 1986. Three Unpublished Ostraca from Gezer. Bulletin of the American Schools of Oriental Research No. 264, pp. 51-60.

Shaus, A., Turkel, E., Piasetzky, E. 2012. Quality evaluation of facsimiles of Hebrew First Temple Period inscriptions. Proceedings of the 10th IAPR International Workshop on Document Analysis Systems.

Shaus, A., Turkel, E., Piasetzky, E. 2012. Binarization of First Temple Period inscriptions - performance of existing algorithms and a new registration based scheme. Proceedings of the 13th International Conference on International Conference on Frontiers in Handwriting Recognition (accepted).

Shaus, A., Finkelstein, I., Piasetzky, E. Avoiding the Eye of the Beholder: Automated Ostraca Facsimile Evaluation. Maarav, Vol 17.1 (forthcoming).

Verhoeven, G., 2008. Imaging the invisible using modified digital still cameras for straightforward and low-cost archaeological near-infrared photography. Journal of Archaeological Science Vol 35, pp. 3087-3100.

Zuckerman, B., 1997. Photography of manuscripts. Oxford Encyclopedia of Archaeology in the Near East Vol 4, pp. 336-347.

Electronic Sources:

[1] Lifepixel. Digital Infrared conversions. (website): http://lifepixel.com. Last accessed: 05.12.2011.

[2] Maxmax. Canon 450D Xsi. (website): http://www.maxmax.com/canon_450d_xsi.htm. Last accessed: 05.12.2011.

[3] Loop Technology. CMOS Sensor Cameras for Digital Vision. (website): http://www.looptechnology.com/cmos-sensor-cameras.asp. Last accessed: 05.12.2011.

[4] Maxmax. 58mm filters. (website): http://www.maxmax.com/aXNite58mm Filters.asp. Last accessed: 05.12.2011.

[5] Midopt. Bandpass filters. (website): http://www.midopt.com/filters.html. Last accessed: 05.12.2011.

[6] Omega optical. precision optical filters (website): http://www.omegafilters.com. Last accessed: 05.12.2011.

[7] Michael Tapes Design. WhiBal White Balance Reference Card. (website): http://michaeltapesdesign.com/whibal.html. Last accessed: 05.12.2011.